Understanding atomic x-ray absorption fine structure in x-ray absorption spectra

1998 J. Phys.: Condens. Matter 10 8753

(http://iopscience.iop.org/0953-8984/10/39/013)

J. Phys.: Condens. Matter **10** (1998) 8753–8770. Printed in the UK PII: S0953-8984(98)94062-0

Understanding atomic x-ray absorption fine structure in x-ray absorption spectra

D E Ramaker†‡‖, B L Mojet§, D C Koningsberger§ and W E O'Grady‡

† Department of Chemistry and Materials Science Institute, George Washington University, Washington, DC 20052, USA

‡ Chemistry Division, Naval Research Laboratory, Washington, DC 20375, USA

§ Department of Inorganic Chemistry, Debye Institute, Utrecht University, PO Box 80083, 3508 TB Utrecht, The Netherlands

Received 12 May 1998, in final form 9 July 1998

Abstract. The origin and important parameters determining the intensity of atomic x-ray absorption fine structure (AXAFS) are described both in chemical and physical terms. A full mathematical derivation is presented and new criteria are given for removal of the background to extract the total χ (EXAFS and AXAFS) from the experimental absorption cross-section. The embedded-atom potential, the interstitial potential and the distribution of the absorber-atom electron density are all found to be important in determining the AXAFS intensity. Application is made to spherical Pt metal clusters, where it is shown that the AXAFS intensity of the central atom is much larger than that of the surface atoms. However, the average AXAFS intensity per platinum atom is found not to depend significantly on cluster size. On the other hand, variation of the metal cluster support does considerably change the intensity as well as the imaginary part of the AXAFS. Hence, AXAFS can be a very useful probe of the effects of metal–support interactions in supported noble-metal catalysts.

1. Introduction

An x-ray absorption spectrum (XAS) reflects the spectral distribution of the excitation cross-section with photon energy [1]. The observed fine structure in the data is the result of interference between the outgoing and backscattered photoelectron waves. These oscillations contain structural information on the number of neighbours around the absorber atom, the identity and distance of those neighbours, and the disorder in the structure of the sample under study. The complete x-ray absorption spectrum consists of an absorption edge, XANES (x-ray absorption near-edge structure) and EXAFS (extended x-ray absorption fine structure).

The Fourier transform (FT) of the EXAFS structure results in a radial distribution function of the neighbouring atoms around the absorber atom. However, often peaks are observed in the distribution function at distances smaller than 1.5 Å from the absorber atom. These cannot be attributed to meaningful bond lengths of neighbouring atoms, as these distances point to a location inside the periphery of the absorber atom itself. In k-space these peaks at low R show themselves as slowly varying sine waves.

As early as 1978, Holland *et al* [2] pointed to the existence of structure in k-space, caused by scattering of the photoelectron off electrons in the periphery of the absorber

‖ E-mail: ramaker@gwu.edu.

0953-8984/98/398753+18$19.50

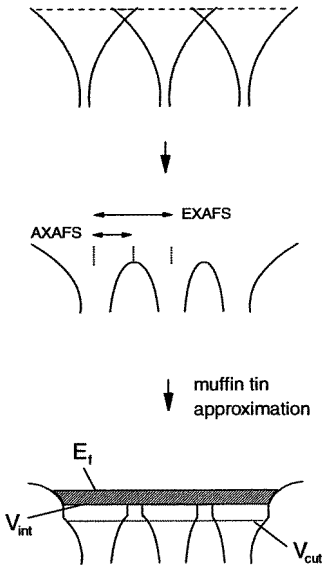

Figure 1. A schematic view of overlapped atomic potentials and the muffin-tin approximation. The EXAFS and AXAFS are indicated along with the potentials $V_{\rm cut}$ and $V_{\rm int}$ as defined in the text. The shaded area indicates occupied itinerant band states.

atom (see figure 1). They called this phenomenon atomic XAFS (AXAFS). Recently, Rehr *et al* [3, 4] attributed the low *R*-peaks mentioned above to AXAFS and showed that this low-frequency oscillatory behaviour could indeed be represented as a sine wave with the usual EXAFS interpretation.

Although a physical interpretation has been given, AXAFS is still controversial since the observed structures in the background have also been attributed to multi-electron excitations [5, 6]. However, the multi-electron excitations present in XAFS data for metals, such as those studied in this work, are expected to be much less pronounced than for the oxide materials which were used in the early studies of AXAFS [3, 4]. Moreover, the characteristics and systematic changes in the observed oscillations, identified as AXAFS, would not be expected if they arose from multi-electron excitations. A systematic change in the AXAFS intensity with the potential applied to a Pt electrode in an electrochemical cell has recently been reported [7]. Wende *et al* also showed that the AXAFS intensity varies with the incident photon angle and sample temperature [8] for N/Cu. Finally, while Holland *et al* [2] and Rehr *et al* [3] used a background-subtraction method in their data analysis that left the AXAFS features in the background, we present a procedure which leaves the AXAFS together with the EXAFS oscillations in $\chi_{\rm total}(k)$. The long-range regular oscillatory behaviour of the AXAFS revealed as a resolved low *R*-peak in the FT varies systematically with chemical changes. Such behaviour strongly suggests that scattering phenomena rather than multi-electron excitations are primarily responsible, even if multi-electron oscillations are also present in the background.

The aim of this work is to elucidate the origin and basis of AXAFS features in x-ray absorption spectra in order to reveal the applicability of AXAFS in understanding chemical effects in catalysis and other fields of chemistry. Specifically, the objectives are

(a) to give a more intuitive physical and chemical interpretation of the AXAFS signals

found in the FT of XAFS data for noble-metal clusters, and ascertain the parameters which are most important in determining the AXAFS intensity;

(b) to describe a suitable experimental background-determination procedure, and

(c) to show, both theoretically and experimentally, that the AXAFS intensity for Pt clusters is nearly independent of their size, but that the intensity is very sensitive to the metal cluster support. This latter point is very important for applications in catalysis and electrochemistry, where the nature of the metal–support interaction is critical to the understanding of the catalytic behaviour.

Figure 1 gives a schematic illustration of the potentials around an absorber atom. Each free-atom potential overlaps with the potential of neighbouring atoms in a solid, so the 'embedded'-atom potential is significantly altered, particularly in the 'bonding' region. When a photoelectron is ejected, it can be either scattered off the potential of a neighbouring atom (EXAFS) or off its own potential (AXAFS) as illustrated. Clearly the AXAFS depends on the nature of the neighbouring atoms and how they are bonded to the absorber.

The FEFF7 code [10] utilized in this work to interpret the AXAFS results makes the well-known muffin-tin approximation. As further illustrated in figure 1, the muffin-tin approximation 'clips' the exact potential at the muffin-tin radius R_{mt} and sets it equal to the interstitial potential V_{int} [2, 3]. Inside R_{mt}, the potential is assumed to be spherical; outside, it is assumed to be flat and zero (i.e. no forces are exerted on the particle in the interstitial region). V_{int} is determined by averaging the potential at R_{mt} of all of the atoms in the cluster, and this determines the zero of energy or the effective bottom of the itinerant band (the nature of V_{cut} will be discussed in section 5). The effect of this approximation is negligible for EXAFS but can be significant for AXAFS as shown previously [2, 3, 7]. Generally, the discontinuity in the potential introduced by this approximation causes the FEFF7 code to overestimate the magnitude of the AXAFS, and shift it slightly to lower R, and we will see this below as well. However, Wende *et al* [8] show that if the muffin tins are allowed to overlap, the AXAFS magnitude, R-range, and phase are all much more in agreement with experiment. We utilize the FEFF7 code here as a tool only to qualitatively explain the trends with changes in chemistry, not to make quantitative comparisons. Thus the use of the FEFF7 code in this work is valid, and we use it without overlapping the muffin tins.

2. The nature of the backscattering in x-ray absorption spectra

It is well known [9] that the backscattering amplitude depends on the atomic number (Z) of the scattering element. To illustrate this, figure 2 shows the backscattering amplitudes

$$F'(k) = S_0^2 \exp(-2R/\lambda) \exp(-2k^2\sigma^2) F(k)$$

in k-space as calculated for Pt–Pt, Pt–O, and Pt–H scattering pairs. All of the calculations reported in this work were performed by means of FEFF7 [10] using Dirac Hara potentials, with an imaginary part of 5 eV which was found to give the best agreement with experimental data [11]. To reveal the resonant nature of the scattering, the binding energies of some core levels in the scattering atoms are also shown in figure 2. The binding energy is converted to k-space according to the normal relation as noted in the figure. It can be seen that the backscattering intensity is enhanced at those photoelectron energy values that are equal to the orbital energies of the respective atoms. Consequently, for hydrogen only one maximum is observed in the backscattering amplitude at low k ($\sim$2 Å^{-1}), after which the scattering dies out quickly. For oxygen two features are visible, one caused by scattering

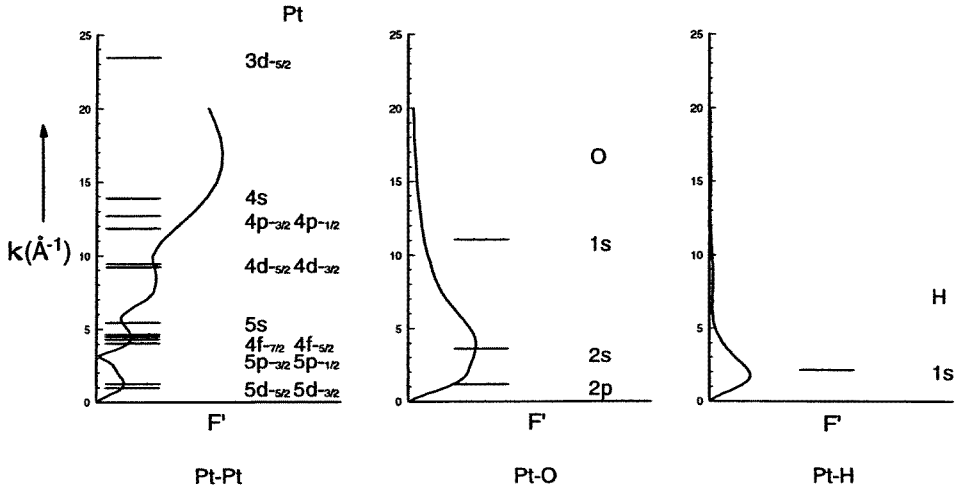

Figure 2. Calculated backscattering amplitudes $F'(k)$ ($F'(k) = kR^2 \times$ amplitude, $A(k)kR^2 = S_0^2 \exp(-2R/\lambda)\exp(-2k^2\sigma^2)F(k)$) and the orbital binding energies, E_{binding}, indicated, for Pt–Pt, Pt–O and Pt–H scattering. E_{binding} is converted to k-space according to $k = \sqrt{\{(2m/\hbar^2)E_{\text{binding}}\}}$.

off the 2p orbitals, and the second by scattering off the 2s orbitals. Around $k = 11$ Å^{-1} a small shoulder is visible due to scattering off the 1s electrons. The backscattering amplitude for Pt shows four maxima caused by respectively, 5d, 5p–4f–5s, 4d and 4p–4s electrons. Consistently with the virial theorem for a Coulomb potential [12], the orbital kinetic energy is approximately equal to minus the binding energy. Thus this figure clearly shows the resonant nature of the scattering; i.e. for maximum scattering, the kinetic energies of the outgoing photoelectron and the bound electrons tend to be equal. The data for Pt–Pt also reveal a large increase in the backscattering cross-section with increasing k-values (or energy).

The photoelectron can also be scattered by the electrons present in the absorber atom. The core electrons (i.e. those at very small distance (R) from the origin of the absorber atom) give rise to the smoothly varying atomic background (μ_{free}) that is observed in x-ray absorption spectra up to large k. When photoelectrons scatter off the inter-atomic potential (i.e. those valence electrons in the periphery of the absorber atom and in the deep valence region) this gives rise to an increased modulation in the atomic background, the so-called AXAFS. Because of the resonant nature of scattering, the AXAFS will necessarily extend only to intermediate ranges in k-space.

The following section presents new criteria for the background-subtraction procedure in XAS data analysis needed to isolate AXAFS and EXAFS oscillations from a complete x-ray absorption spectrum.

3. Background subtraction from x-ray absorption data

The AXAFS features arise from the difference between a free-atom potential and an embedded-atom potential. As was shown in figure 1, the embedded potential exhibits a 'roll-over' shape, which is absent for the free atom. Consequently, the embedded atom has an atomic absorption μ_a, which can be viewed as a combination of the atomic background of the free atom (μ_{free}) and the AXAFS signal (χ_{atomic}) which results from alteration of the

potential by a chemical environment other than vacuum:

$$\mu_a = \mu_{\text{free}}(1 + \chi_{\text{atomic}}). \tag{1}$$

The atomic absorption μ_a is related to the total x-ray absorption spectrum μ_{total} according to [1]

$$\chi_{\text{neighbours}} = \frac{\mu_{\text{total}} - \mu_a}{\mu_a} \tag{2}$$

which isolates $\chi_{\text{neighbours}}$ attributed to EXAFS scattering. Including equation (1) in (2) results in the following expression for the total absorption coefficient [3]:

$$\mu_{\text{total}} = \mu_{\text{free}}(1 + \chi_{\text{atomic}})(1 + \chi_{\text{neighbours}}) = \mu_{\text{free}}(1 + \chi_{\text{total}}). \tag{3}$$

Previous studies on AXAFS focused on removing the complete atomic 'background' μ_a from experimental data (i.e. extraction of $\chi_{\text{neighbours}}$) either by established criteria [14] or more recently by iterative analysis. The latter required the assumption that the significant information contained in $\chi_{\text{neighbours}}$ (such as the backscattering, Debye–Waller and loss factors, and even some aspects of the atomic structure) is known or can be accurately calculated [13] .

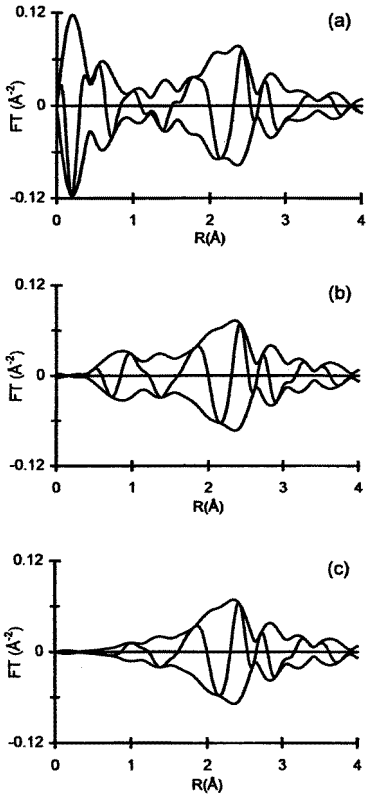

Figure 3. The Fourier transform ($k^1\chi_{\text{total}}$; Δk: 3.0–13.5 Å^{-1}) of experimental data from Pt/LTL (K/Al molar ratio = 0.96) after three different levels of background smoothing. (a) The free-atom signal is left in the data. (b) The free-atom scattering is removed, while the AXAFS signal is kept. (c) Background removal according to earlier criteria.

There are three reasons why we prefer not to use the iterative background-subtraction method in the data analysis of the supported noble-metal catalysts utilized in this work. First, in order to display the relation between EXAFS and AXAFS, the two signals should be in the same Fourier transform, e.g. the AXAFS should be kept in χ_{total} instead of in the background. Second, if one applies an iterative background subtraction, some aspects of the local structure around the absorber element have to be known; otherwise it is not possible to ascertain whether the complete EXAFS scattering has been isolated. The previously proposed iterative background-subtraction techniques were based on the premise of knowing the structure of the bulk crystalline compounds under study. In our case, we have small supported metal particles with unknown contributions from the support. Third, as can be seen from equation (3), there is a modulation of the type $\chi_{\text{neighbour}} * \chi_{\text{AXAFS}}$, the so-called cross-term. The cross-term is small as long as χ_{AXAFS} is small, but we find at least in our theoretical results (which overestimate χ_{AXAFS}) that the AXAFS signal is at least 50% of the 'normal' EXAFS amplitude, thus introducing a cross-term with significant amplitude in the EXAFS region. Consequently, it is not expedient in our case to utilize the iterative background-removal and fitting procedures outlined previously.

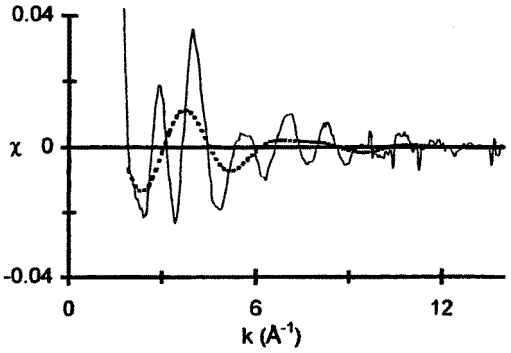

Figure 4. The experimental EXAFS for Pt/LTL(0.96) (χ_{total}, solid line) and the back-transformed Fourier-filtered AXAFS signal (χ_{AXAFS}, dotted line) from figure 3(b) (Δk: 1.9–13.8 Å^{-1}; ΔR: 0.14–1.58 Å).

A new background-subtraction method is now presented that is based on three criteria. We use the normal method of applying a cubic spline to fit the atomic background [14]. The objective is to remove only μ_{free}, leaving χ_{AXAFS} in the data. Figure 3 shows the effect of three different levels of smoothing used for the background subtraction from an experimental x-ray absorption spectrum obtained for a Pt/LTL catalyst [11, 15]. In figures 3(a) to 3(c) the smoothing parameter is lowered in such a way that:

(a) a considerable amount of the free-atom absorption is left in χ, which is visible at R close to zero in the Fourier transformation, and tailing off to higher distances;

(b) almost all free-atom scattering is removed, but the AXAFS signal at $R = 1$ Å is still present in the data; and

(c) all intensity at low R-values in the Fourier transform is removed (i.e. μ_a is removed) according to the background criteria used previously [14].

The optimum background subtraction is to retain the AXAFS in the Fourier transform as shown in figure 3(b). Three criteria are used to determine a consistent background.

(1) Diminish as much as possible the free-atom contribution at $R < 0.5$ Å.

(2) At the same time, leave the EXAFS signal at $R > 1.54$ Å unreduced.

(3) Check this procedure both in k^1- and k^3-weighting for different k-ranges, including low k-values (e.g. k down to 1.5 Å^{-1}).

The last criterion is important to ensure that no EXAFS signal is removed from the data. Previously, it was often required to remove about 10% of the intensity of this peak in order to eliminate the peak at 1 Å (figure 3(c)). Now no decrease in this signal is allowed, yet the free-atom contribution is, one hopes, completely removed from the data. The signal remaining at small R is the difference between the scattering for the embedded atom in a chemical environment and the free atom.

Figure 4 shows the AXAFS in k-space after Fourier filtering (ΔR: 0.14–1.58 Å) the signal around $R = 1$ Å from figure 3(b). This AXAFS contribution has a low-frequency long-wavelength oscillation, with high amplitude at low k-values (=low photoelectron kinetic energy). The contribution still has some amplitude at higher energies, indicating that χ_{AXAFS} has a significant range, but because of the long wavelength only two or three oscillations are visible before it dies out. Note that χ_{AXAFS} dies out more quickly than $\chi_{\mathrm{Pt-Pt}}$ as expected from the discussion in section 2.

4. Atomic potentials in metal clusters

In order to understand the physical meaning of AXAFS, the atomic potentials obtained from FEFF7 for the absorber as a free atom and an embedded atom are shown in figure 5(a). The potentials were calculated for a free atom, simulated by a Pt–Pt scattering pair at very long distance (4.75 Å), and a Pt-13 atom cluster with FCC structure. The Pt–Pt distance in the cluster was chosen to be 2.74 Å, since this is the metal–metal distance found after analysis of small supported platinum clusters in Pt/LTL [15, 16]. Three potentials are given in figure 5(a), namely V_{free} (for a free atom), V_{surface} (for a surface atom of a 13-atom cluster), and V_{central} (for a central atom of a 13-atom cluster). The central atom shows a lower potential than the free atom due to overlap with the potential of neighbouring atoms. The surface atom has a potential which is located between that of the free atom and the central atom, as would be expected from the fact that fewer neighbours contribute to the 'roll-over' of the potential. The potential for R close to 0 is not shown here as it approaches $-\infty$ at $r = 0$. In figure 5(a), V_{int} (the average interstitial potential) as calculated by FEFF7 is indicated for the 13-atom cluster. Furthermore, the muffin-tin radius is pointed out for the central and surface atoms. V_{int} meets the electron potential exactly at the muffin-tin radius R_{mt} for the surface atom (see point A figure 5(a)), which means that there is no discontinuity between the surface-absorber and interstitial potentials at R_{mt}. For the central atom, R_{mt} and V_{int} meet above the absorber potential (V_{central}) at point B. Thus a discontinuity is present between the central-atom potential and the interstitial potential. This discontinuity points to a potential gradient from the inner core of the metal particle to the outer surface atoms where no discontinuity is observed.

Such a potential gradient can be understood from a chemical viewpoint. The central atom has more neighbouring atoms than a surface atom; hence more of its electrons are involved in chemical bonds. Consequently, the electrons will be located at higher binding energies (more negative energy), and the electron density will increase at larger distance from the origin of the absorber atom (i.e. between the two bonding atoms). The spherical-potential requirement in the muffin-tin approximation simulates this chemical effect by lowering the potential (V_{central}) from the interstitial potential (V_{int}) and rolling it over (i.e. making more curvature than the surface-atom potential).

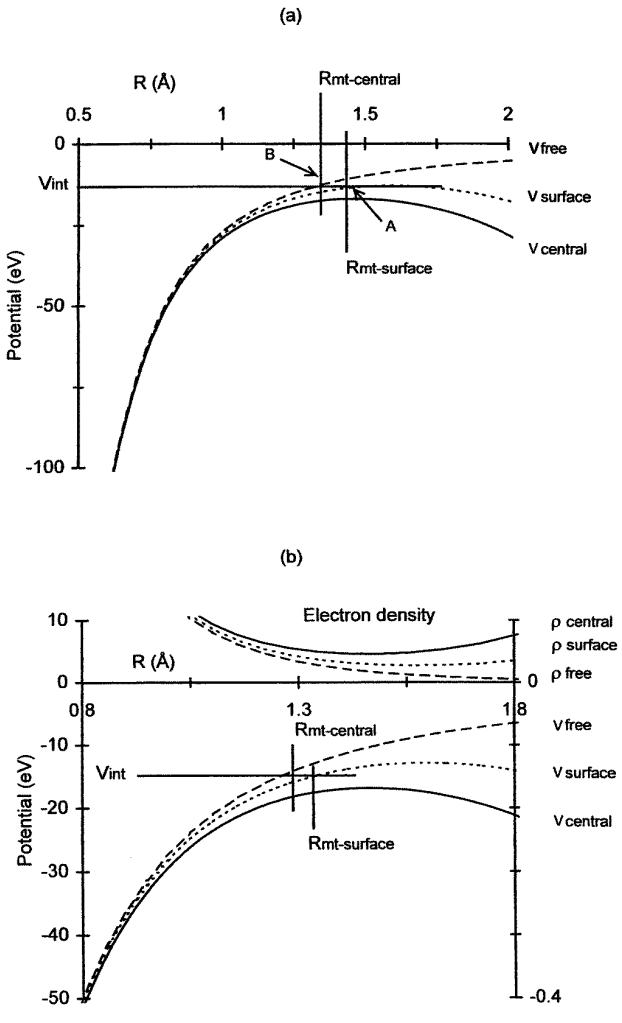

Figure 5. Atomic potentials as calculated by means of FEFF7 for a 13-atom spherical Pt cluster and for a free atom calculated as described in the text. (a) Atomic potentials, $V_e(R)$, with R_{mt} and V_{int} indicated. (b) A close-up of (a) together with radial electron density distribution $\rho(R)$.

Figure 5(b) shows a close-up of figure 5(a) together with the radial electron distributions for the free, central and surface atoms. The electron densities at larger distances increase from the free atom, to the surface, and to the central atom exactly as anticipated above.

Three variables appear to be important for the AXAFS amplitude in XAS:

(1) the area difference between the atomic potentials V_{free} and V_e;
(2) the interstitial potential V_{int}; and
(3) the electron density distribution with energy.

To clarify this, a mathematical description of AXAFS is given below, starting from the absorption cross-section as originally given by Holland *et al* [2]. It is shown that this approach leads to the physical derivation for AXAFS as given by Rehr *et al* [3].

5. Mathematical description of AXAFS

The absorption cross-section utilizing Fermi's golden rule and the dipole approximation is given by

$$\mu(k) = \mu_a(1 + \chi_{\text{neigbours}}(k)) = 4\pi^2\alpha\omega[1 + \chi_{\text{neighbours}}(k)]|\mathcal{L}(k)|^{-2}|M|^2. \quad (4)$$

Here, ω is the photon energy, k the outgoing photoelectron wavevector, and α the hyperfine constant. Holland *et al* [2] argued that M, the atomic dipole matrix element, is a relatively slowly varying function of k compared with $\mathcal{L}$, so M will be regarded as a constant in this derivation; thus

$$\mu_{\text{atomic}}(k) \propto |\mathcal{L}(k)|^{-2} \quad (5)$$

in which $\mathcal{L}(k)$ is the so-called Jost function defined in terms of the regular solution $\phi_l(kr)$ of the Schrödinger equation and the embedded potential V_e [17]:

$$\mathcal{L}_l(k) = 1 + \frac{2m}{k\hbar^2}\int_0^\infty h_l^+(kr)V_e(r)\phi_l(kr)\,\mathrm{d}r = 1 + A_{V_e}. \quad (6)$$

The wavefunction ϕ is asymptotically defined by

$$\phi_l(kr) \underset{r\to\infty}{\longrightarrow} \frac{\mathrm{i}}{2}\left[\mathcal{L}_l(k)h_l^-(kr) - \mathcal{L}_l(k)^*h_l^+(kr)\right] \quad (7)$$

where $h_l^\pm(kr)$ are the outgoing and incoming wavefunctions for a free particle. The normalized wavefunction $\psi_l(kr)$ is then equal to $\phi_l(kr)/\mathcal{L}_l^*(k)$ and shows the following behaviour:

$$\psi_l(kr) \underset{r\to\infty}{\longrightarrow} \frac{\mathrm{i}}{2}[h_l^+(kr) - s_l(k)h_l^-(kr)] \quad (8)$$

where $s_l(k)$ is the scattering matrix element equal to $\exp(-2\mathrm{i}\delta)$. Here, $\psi_l(kr)$ represents the outgoing photoelectron wave along with the backscattered AXAFS wave.

The general equation (equation (6)) for the Jost function given above is an integral equation which can be expanded into a Born-type series [17]:

$$\mathcal{L}_l(k) = 1 + \sum_l^\infty \mathcal{L}_l^{(n)}(k). \quad (9)$$

In zeroth order the Jost function is equal to one, and in the first Born approximation, one keeps just the first term in the series. In this case the Jost function is given by equation (6), but with $\phi_l(kr)$ asymptotically equal to i/2 times the outgoing and incoming waves for the free particle,

$$\phi_l(kr) \to (\mathrm{i}/2)[h_l^-(kr) - h_l^+(kr)].$$

Since the exact wavefunction is closer to the wavefunction for the free atom than it is to that of a free particle, it is more appropriate and accurate here to use the distorted-wave Born (DWB) approximation, in which case $\mathcal{L}_l(k)$ can be expressed as

$$\mathcal{L}_l(k) = \mathcal{L}_l^{FA} + \sum_l^\infty \mathcal{L}_l^{(n)FA}(k) \quad (10)$$

where $\mathcal{L}_l^{FA}(k)$ is the Jost function for the free atom (FA). Now in zeroth order the Jost function is equal to $\mathcal{L}_l^{FA}(k)$, and in the first DWB approximation the Jost function is given by

$$\mathcal{L}_l(k) = \mathcal{L}_l^{FA} + A_{V_e - V_{TFA}}. \quad (11)$$

Here, $A_{V_e-V_{TFA}}$ now involves only the outgoing wavefunction for the free atom (i.e. $\phi_l(kr) \rightarrow (\mathrm{i}/2)h^+_{l,FA}(kr)$, which is asymptotically similar to the expression for a free particle but with the proper phase included). Equation (11) indicates that the Jost function for a particle in the embedded atom is similar to that for a particle in the free atom, except for a correction term, A. The correction term now involves the difference between the embedded-atom potential V_e and the free-atom potential V_{FA}, where the free-atom potential must have the same zero of energy as the embedded-atom potential—hence the notation $V_e - V_{TFA}$. In the muffin-tin approximation, the zero of energy corresponds to V_{int}, the average of the interstitial potentials, so a muffin-tin-like approximation is also made for the free atom; i.e. the free-atom potential is set to zero when it goes above V_{int}. We shall refer to this potential as the 'truncated' free-atom potential V_{TFA} from here on.

Now, in order to evaluate the absorption cross-section (equation (5)), a Taylor series is used:

$$\mu(k) \propto |\mathcal{L}(k)|^{-2} \approx [L^{FA}]^{-2}\left[1 + \frac{A_{V_e-V_{TFA}}}{\mathcal{L}^{FA}}\right]^{-2} \approx [L^{FA}]^{-2}(1 - \mathrm{Re}(A_{V_e-V_{TFA}})) \tag{12}$$

which defines

$$[\mathcal{L}^{FA}]^{-2}(1 - \mathrm{Re}(A_{V_e-V_{TFA}})) = \mu_{FA}(1 + \chi_{\mathrm{atomic}}). \tag{13}$$

Keeping only terms linear in $V_e(r)$ (consistently with the first DWB approximation), χ_{atomic} is given by

$$\begin{aligned}\chi_{\mathrm{atomic}} &\approx \frac{-2m}{k\hbar^2}\,\mathrm{Im}\int_0^{R_{\mathrm{mt}}} h_l^{+,FA}(k_e r)[V_e(r) - V_{TFA}]h_l^{+,FA}(k_e r)\;\mathrm{d}r \\ &\approx \frac{-2m}{k\hbar^2}\,\mathrm{Im}\int_0^{R_{\mathrm{mt}}} \mathrm{e}^{2\mathrm{i}k_e r + 2\mathrm{i}\delta_l}(V_e(r) - V_{TFA})\;\mathrm{d}r\end{aligned} \tag{14}$$

with

$$h_l^{+,FA}(kr) \rightarrow \mathrm{e}^{\mathrm{i}kr + \mathrm{i}\delta_l}.$$

Our final equation above is essentially the result obtained by Rehr *et al* [3].

Now we take a phase-weighted FT of $k\chi_{\mathrm{atomic}}$:

$$\begin{aligned}\mathrm{FT}(k_f \mathrm{e}^{-2\mathrm{i}\delta}\chi_{\mathrm{atomic}}) &= \sqrt{\frac{2}{\pi}}\int_0^{\infty} \mathrm{e}^{-2\mathrm{i}k_f R}k_f \mathrm{e}^{-2\mathrm{i}\delta}\chi_{\mathrm{atomic}}\;\mathrm{d}k_f \\ &= \frac{-2m}{\hbar^2}\int_0^{R_{\mathrm{mt}}}(V_e(r) - V_{TFA})\sqrt{\frac{2}{\pi}}\int_0^{\infty}\mathrm{e}^{-2\mathrm{i}k_f R}\,\mathrm{Im}(\mathrm{e}^{2\mathrm{i}k_e r})\;\mathrm{d}k_f\;\mathrm{d}r\end{aligned} \tag{15}$$

with

$$\sqrt{\frac{2}{\pi}}\int_0^{\infty}\mathrm{e}^{-2\mathrm{i}k_f R}\,\mathrm{Im}(\mathrm{e}^{2\mathrm{i}k_e r})\;\mathrm{d}k_f \approx \delta(R - r)$$

(when $k_e \approx k_f$; it is negligible otherwise). Thus,

$$\mathrm{FT} \propto [V_e(R) - V'_{TFA}] * \Gamma \tag{16}$$

where the $* \Gamma$ indicates that the potential difference is broadened by an amount Γ because in practice a finite FT must be taken. The prime on V_{TFA} indicates that a further truncation of the free-atom potential occurs as a result of the Fourier transform and the differences in zero-point energies between theory and experiment. In equation (15), k_f is relative to the

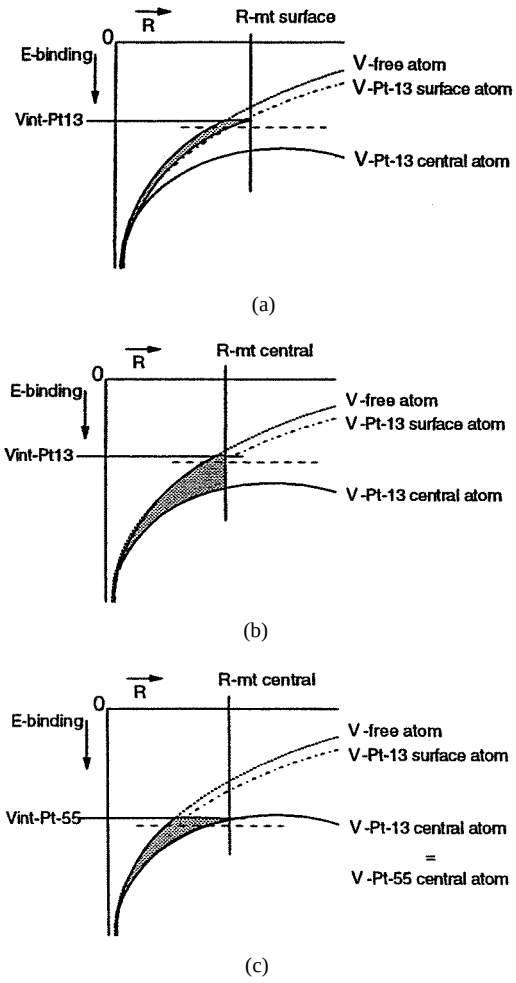

Figure 6. A schematic representation of the atomic potentials $V_e(R)$ for a 13-atom or 55-atom spherical Pt cluster in comparison with a free Pt atom. The shaded area in each case indicates the difference $V_e - V_{TFA}$ and roughly reflects the relative AXAFS intensity expected. The dashed line indicates the cut-off for effective AXAFS scattering as described in the text. (a) The Pt-13 surface-atom case, (b) the Pt-13 central-atom case, and (c) the Pt-55 central-atom case.

Fermi level which is the usual zero reference for the experimental data, while k_e is relative to the embedded-atom zero, namely V_{int}. Therefore

$$k_f = \sqrt{k_e^2 + \frac{2m}{\hbar^2}(E_f - V_{\text{int}})}$$

and $k_f \simeq k_e$ only when k_e^2 is larger than $(2m/\hbar^2)(E_f - V_{\text{int}})$. Because of the orthogonality of the exponential functions for different k when $R = r$, the integral in equation (15) will be negligible at least down to $V_{\text{int}} - |V_{\text{int}} - E_f|$. Thus the effective cut-off potential V_{cut} is not V_{int} but even lower, namely $V_{\text{cut}} = 2V_{\text{int}} + |E_f|$. This is indicated by the dotted lines in the figures to follow and in figure 1.

In the final expression for the Fourier transform, equation (16), the dipole matrix element, the M-factor, mentioned at the beginning of this section and the constants of

equation (4) have to be included back in, but since these factors are slowly varying they do not alter the conclusions reached here. This derivation indicates that the phase-weighted FT of $k * \chi_{\text{atomic}}$ essentially results in a direct plot of the potential difference between the embedded atom and the truncated free atom. As a result, the AXAFS peak appearing at low R in the FT can be a direct measure of changes in atomic potential resulting from chemical variations in a system. This indeed has already been suggested by the changes observed with applied potential on a Pt electrode, and in a Pt/Ru alloy [7]. The finite FT should yield some broadened and truncated potential difference, with a maximum near R_{mt} or less, and decreasing in intensity as R goes to zero as experimentally observed.

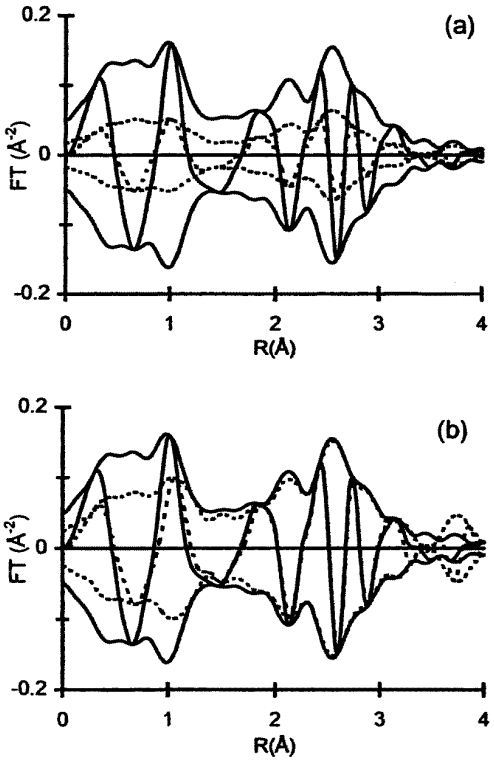

Figure 7. (a) Fourier transforms ($k^1\chi_{\text{total}}$; Δk: 3–15 Å^{-1}) of the FEFF7-calculated spectrum for a Pt-13 central atom (solid line) and a Pt-13 surface atom (dotted line). (b) Fourier transforms (k^1; Δk: 3–15 Å^{-1}) of the calculated χ_{total}-spectrum for a Pt-13 central atom (solid line) and a Pt-55 central atom (dotted line).

The above mathematical derivation shows that the AXAFS signal is proportional to the potential difference between the embedded atom and the truncated free atom. This potential difference is shaded for a surface atom on the 13-atom cluster in part (a) of figure 6. Figure 6(b) shows the same potential difference for the central atom in a Pt-13 atom cluster. There is a clear difference between the $V_e - V_{TFA}$ integrated areas for these two cases, with the central-atom area much larger. This suggests that the AXAFS for the central atom should be larger than that for the surface Pt-13 atom. Analysis of the data generated by FEFF7 for these two cases shows that there is indeed an amplitude difference in the AXAFS signal (figure 7(a)), with the central-atom signal larger. This reveals the effect of

the potential overlap with neighbouring atomic potentials (resulting in V_e) on the AXAFS intensity.

Figure 6(c) shows the importance of the position of the interstitial or cut-off potential (V_{cut}). Here, the potential of the central atom in a Pt-55 cluster (which is identical to that of the central atom in a Pt-13 cluster) and V_{int} for the Pt-55 cluster are shown. The interstitial potential, V_{int}, decreases for the larger cluster because the central-to-surface-atom ratio is much larger in the 55-atom cluster (approximately 31/55 compared with 1/13), and therefore the more coordinated central atoms dictate the position of V_{int}. Alternatively, V_{int} also turns out to be somewhat similar to the energy levels of a particle in a box when the box becomes larger. Figure 7(b) shows the Fourier transforms of the spectra calculated by means of FEFF7 for the Pt-55 central atom and the Pt-13 central atom. It can be seen that the AXAFS for the Pt-13 central atom is larger than that of the Pt-55 central atom, which is also consistent with the relative $V_e - V'_{TFA}$ areas (figures 6(b) and 6(c)).

It should be clear that the interstitial potential, V_{int}, and the overlapped potential are important for determining the final amplitude of the AXAFS. But the distribution of the electron density also has a substantial influence on the atomic scattering intensity. Chemical bonding with neighbouring atoms causes the difference in electron density from that in the free atom, as was explained above. To understand the effect of $\rho(E)$ on the AXAFS intensity, we examine AXAFS from another perspective, where changes in the electron density will be more intuitive.

6. Physical and chemical points of view

The interpretation of the origin of AXAFS scattering in x-ray absorption data has been translated to both chemical and physical points of view in figure 8. There is no difference in the assumptions or fundamental description, but we want to provide an interpretation of the mathematical results in a more physical and chemical picture. The physical representation primarily understands chemical bonding and electrons as potentials or forces on the electron; these are depicted on the left-hand side of the figure. A more chemical description considers the electrons as scatterers, whereby the density of states is more intuitive (the right-hand side of figure 8). In the middle section, the picture of chemical bonding by formation of new molecular orbitals is shown.

Three situations can be distinguished. At the top, the free atom is depicted with the valence electron density concentrated at the 'Fermi level' (the highest occupied atomic orbital). The AXAFS due to scattering off valence electrons is now very small, because the electrons are concentrated at the Fermi level with very low kinetic energies. To get appreciable scattering inside the atom from the valence electrons, it is necessary that the electrons have a significant binding energy (i.e. kinetic energy) as the photoelectron also has a reasonable kinetic energy.

The scattering is most pronounced when the kinetic energies match for the bound valence electrons and the photoelectron, as illustrated in figure 2. Hence the electrons located very near the Fermi level will not contribute significantly to the AXAFS signal. When neighbours are bonded to a free atom, some of the electrons go into bonding orbitals, which is simulated by the overlap of the potentials in the physical point of view and a little lowering of V_{int}. In chemical terms, the local density of states (LDOS) around the Fermi level is broadened and moved to higher binding (kinetic) energies, and at larger distance from the core (i.e. between the atoms) the electron density increases. Non-bonding electrons left on the platinum atoms determine the Fermi level. Finally, when full coordination is reached, a bulk situation is created and a full band structure appears, which is depicted in the lower part of the figure.

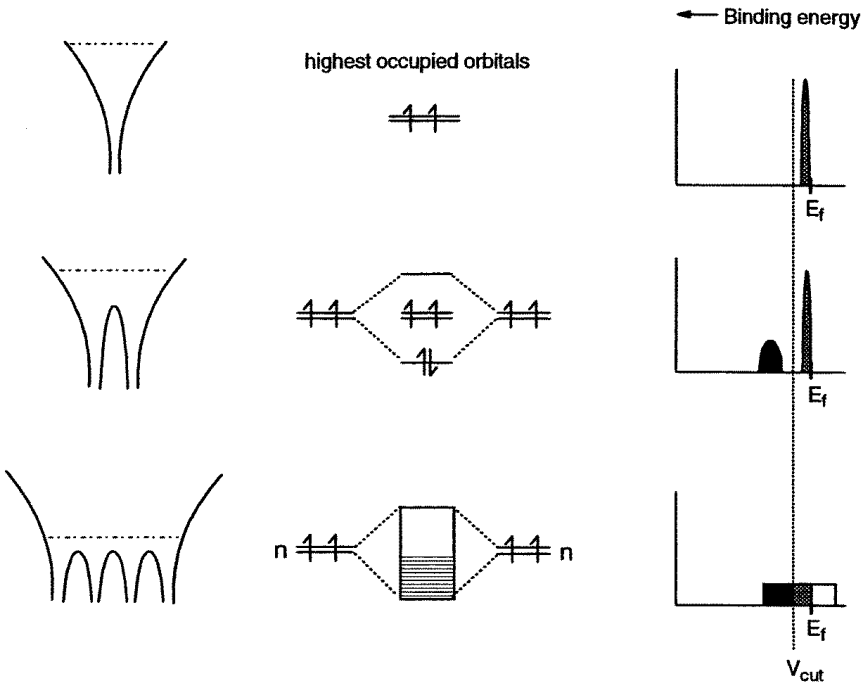

Figure 8. A schematic illustration of the origin of AXAFS from either the 'physical' potential scattering point of view (left-hand side) or 'chemical' electron scattering point of view (right-hand side). The middle section illustrates the formation of molecular orbitals or bands which occurs when the atomic potentials overlap. The vertical dashed line on the right indicates V_{cut} as described in the text. The lightly shaded area indicates the occupied density of states (DOS). Heavily shaded areas indicate the effective DOS for AXAFS scattering.

The effect of the electron energy distribution can now be understood. We have already illustrated the resonant character of the scattering in figure 2. V_{int} is effectively the zero of energy for the delocalized electrons in the conduction band of the metal. The photoelectrons can only be excited to states above the Fermi level several eV above V_{int}. The conduction band has a width essentially proportional to the separation between E_f and V_{int}. The AXAFS is caused by scattering off the localized electrons around the periphery of the atom, and only those electrons with kinetic energies similar to the photoelectrons are capable of doing this. Thus only those localized electrons with sufficient binding energy below V_{int} will be effective in scattering.

These arguments give an intuitive interpretation to the mathematical truncation of the free-atom potential at V_{cut} as discussed above. We have indicated an arbitrary 'cut-off' point below V_{int} to illustrate this effect (dashed lines in figure 6). Only the shaded area below this cut-off is effective in producing AXAFS in this picture. Figure 6 then reveals that a greater percentage of the shaded area in the potential difference plots is 'ineffective' as regards scattering. Thus the magnitude of the AXAFS is not directly proportional to the total shaded area in the potential plots, but rather to the shaded area below the 'dotted' cut-off lines. Of course, the turning on of the scattering is gradual, but the cut-off helps us to better indicate this effect graphically. This cut-off line is also indicated in figure 8 by the dotted lines in the schematic DOS plots. Here only the area below the cut-off line is heavily shaded to more graphically illustrate those electrons that cause the AXAFS scattering.

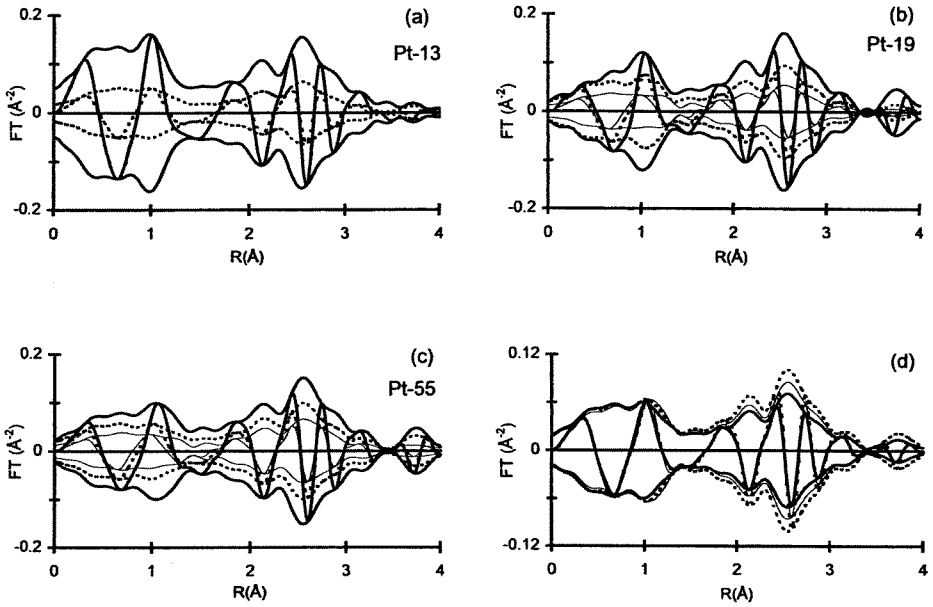

Figure 9. Fourier transforms ($k^1\chi_{\text{total}}$; Δk: 3–15 Å^{-1}) of FEFF7 results. (a) The Pt-13 central atom (solid line) and Pt-13 surface atom (dotted line). (b) The Pt-19 central atom (solid line), Pt-19 first-shell atom (dotted line), and Pt-19 surface atom (thin solid line). (c) The Pt-55 central atom (solid line), Pt-55 third-shell atom (dotted line), and Pt-55 surface atom (thin solid line). (d) The total signal expected after proper weighting of individual shells in each cluster; Pt-13 (solid line), Pt-19 (thin solid line), and Pt-55 (dotted line).

7. Comparison of theory with experimental results

It was shown above that the AXAFS for surface atoms has a different intensity than the AXAFS signal for the middle atom of a 13-Pt-atom cluster. This suggests that the particle size might have an influence on the AXAFS intensity, since each particle consists of different ratios of middle atoms versus surface atoms. However, figure 9 shows that this is not the case when a full x-ray absorption experiment is simulated. Figures 9(a) to 9(c) show Fourier transforms of the $\chi(k)$ of the surface, middle and central atoms of Pt clusters with FCC structure, ranging from 13 (one shell) to 55 (four coordination shells) atoms. In these calculations, each shell was assigned a unique potential. The intensity of the AXAFS signal for a central atom decreases with increasing cluster size and converges to the value of the Pt-55 cluster; that for a surface atom remains relatively constant with cluster size. Larger clusters were also calculated, but they resulted in AXAFS signals similar to that of the Pt-55 atom cluster. Figure 9(d) shows the average AXAFS obtained after appropriately weighting the individual contributions from each coordination shell. Only small variations can be seen in the shapes and shifts in the imaginary part of the AXAFS signals, but no large changes occur in the average AXAFS intensity. This somewhat surprising fact—that the average AXAFS intensity is hardly dependent on the cluster size—is caused by the decrease in AXAFS intensity for the inner atoms with increasing metal particle size. Figure 7(b) already showed that the centre atom of the Pt-55 atom cluster has about half the AXAFS intensity as compared to the central atom of the Pt-13 cluster. If the AXAFS intensity of surface and bulk atoms had remained similar as cluster size increased, an increase in average

AXAFS amplitude would have been expected, since the interior-to-surface-atom ratio would decrease. However, with increasing particle size the AXAFS of the interior atoms decreases, resulting in the observed similar AXAFS intensities. As the interior/surface ratio goes to infinity (i.e. for bulk Pt foil), the average intensity will equal that of a bulk interior atom, which should be smaller than that of Pt-55. This suggests a very slow asymptotic decrease in the intensity with cluster size.

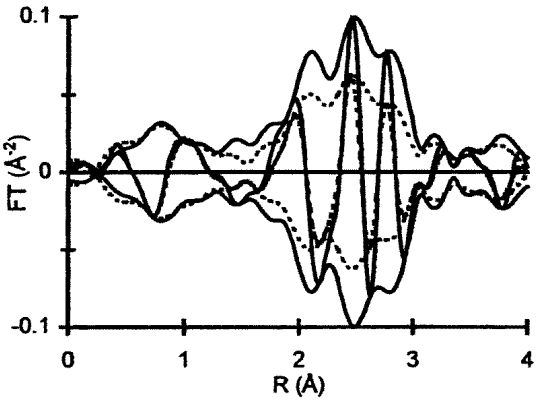

Figure 10. Comparison of Fourier transforms ($k^1\chi_{\text{total}}$; Δk: 3–14 Å^{-1}) of experimental data for Pt clusters supported in Y zeolite catalysts with different average particle sizes: $N_{\text{Pt}-\text{Pt}}$(first shell) = 6 (solid line) and $N_{\text{Pt}-\text{Pt}}$(first shell) = 4.2 (dotted line).

Experimental XAFS data also reveal that the AXAFS intensity is not particle size dependent. Figure 10 shows the Fourier transforms for platinum particles supported on zeolite Y with two different coordination numbers in the first Pt–Pt coordination shell at $R = 2.75$ Å. It can be clearly seen that the intensity, shape, and imaginary parts of the AXAFS remain very similar, although the amplitude in the first EXAFS coordination shell changes.

Although the particle sizes differ, EXAFS is a bulk technique that probes all atoms of a specific element equally, and leads to the result that particle size effects cannot be observed via the experimentally obtained AXAFS intensity. Since in practice it is hard to synthesize series of catalysts with equal particle sizes, this observation, nevertheless, has the advantage that other effects, like the well-established metal–support interaction in catalysis, might be detected by examining the AXAFS signals [18]. Figure 11 shows the spectra of three different samples, namely a Pt foil, Pt/Y of figure 10, and a Pt/LTL catalyst. Comparing the AXAFS intensity of platinum particles on different supports shows that there are differences in both intensity and shape. The imaginary parts in the AXAFS region are very different for the three samples. As indicated above from theory and experiment, the particle size does not significantly influence the AXAFS intensity. We conclude, for this reason, that the chemical environment definitely has an influence on the AXAFS, and thus that changes in the chemical environment can be probed with AXAFS signals. This will be shown more explicitly in a following study [18]. Such a chemical probe will exist as long as the changes do not average out over the whole sample, as was observed for the case of changing metal particle sizes.

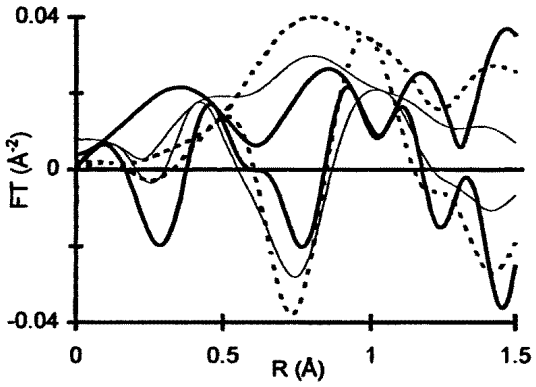

Figure 11. Comparison of Fourier transforms (amplitude and imaginary part) ($k^1\chi_{\text{total}}$; Δk: 3–14 Å^{-1}) of experimental data for supported platinum particles: Pt foil (thin solid line), Pt/Y (dotted line), and Pt/LTL (solid line).

8. Conclusions

The origin and important parameters determining the intensity of atomic XAFS have been described, and can be clearly understood both in chemical and physical terms. The fact that the overlapped atomic potential (V_e), interstitial potential or cut-off potential (V_{int} or V_{cut}), and electron density distribution ($\rho(E)$) are important for the AXAFS intensity reveals that AXAFS can be used to monitor changes in the electronic structure of the absorber atom.

In view of this, it was shown that the AXAFS intensity of central atoms is much larger than that of surface atoms in spherical platinum clusters. In spite of this, the average AXAFS intensity per platinum atom was not found to depend substantially on cluster size; however, variation of the metal cluster support produced significant changes in intensity as well as in the imaginary part of the AXAFS. We conclude, therefore, that AXAFS can be a very useful probe of the effect of metal–support interactions in supported noble-metal catalysts.

Acknowledgment

Support by the Office of Naval Research for D E Ramaker and W E O'Grady is gratefully acknowledged.

References

[1] Koningsberger D C and Prins R (ed) 1988 *X-ray Absorption* (New York: Wiley)
[2] Holland B W, Pendry J B, Pettifer R F and Bordas J 1978 *J. Phys. C: Solid State Phys.* **11** 633
[3] Rehr J J, Booth C H, Bridges F and Zabinsky S I 1994 *Phys. Rev.* B **49** 12 347
[4] Rehr J J, Zabinsky S I, Ankudinov A and Albers R C 1995 *Physica* B **208+209** 23
[5] Filipponi A and Di Cicco A 1996 *Phys. Rev.* B **53** 9466
[6] Rehr J J, Booth C H, Bridges F and Zabinsky S 1996 *Phys. Rev.* B **53** 9568
[7] O'Grady W E, Ramaker D E and Qian X 1997 *J. Phys. Chem.* B **101** 5624
[8] Wende H, Srivastava P, Chauvistré R, May F, Bakerschke K, Arvanitis D and Rehr J J 1997 *J. Phys.: Condens. Matter* **9** L427
[9] Vaarkamp M, Linders J C and Koningsberger D C 1995 *Physica* B **208+209** 159

[10] Zabinsky S I, Rehr J J, Ankudinov A, Albers R C and Eller M J 1995 *Phys. Rev.* B **52** 2995
[11] Mojet B L 1997 *PhD Dissertation* Utrecht University
[12] Levine I N 1993 *Quantum Chemistry* 3rd edn (Boston, MA: Allyn and Bacon) ch 14
[13] Li G G, Bridges F and Brown G S 1992 *Phys. Rev. Lett.* **68** 1609
[14] Cook J W Jr and Sayers D E 1981 *J. Appl. Phys.* **52** 5024
[15] Mojet B L, Miller J T and Koningsberger D C 1998 submitted
[16] Vaarkamp M, Modica F S, Miller J T and Koningsberger D C 1993 *J. Catal.* **144** 611
[17] Taylor J R 1983 *Scattering Theory: the Quantum Theory of Nonrelativistic Collisions* (Malabar, FL: Krieger)
[18] Mojet B L, Miller J T, Ramaker D E and Koningsberger D C 1998 in preparation